# High-conducting Bi4V1.8Cu0.2-xSbxO10.7+3x/2 ceramics: Structural, microstructural, electrical and optical properties

Wafaa Mhaira, Abdelmajid Agnaou, Rachida Essalim, Fabrice Mauvy, Mohamed Zamama, Maati Alga, Abdelaziz Ammar

▶ **To cite this version:**

Wafaa Mhaira, Abdelmajid Agnaou, Rachida Essalim, Fabrice Mauvy, Mohamed Zamama, et al.. High-conducting Bi4V1.8Cu0.2-xSbxO10.7+3x/2 ceramics: Structural, microstructural, electrical and optical properties. Ceramics International, 2023, 49 (23, Part B), pp.39205-39213. ⟨10.1016/j.ceramint.2023.09.264⟩. ⟨hal-04237809⟩

**HAL Id: hal-04237809**

**https://hal.science/hal-04237809v1**

Submitted on 11 Oct 2023

**HAL** is a multi-disciplinary open access archive for the deposit and dissemination of scientific research documents, whether they are published or not. The documents may come from teaching and research institutions in France or abroad, or from public or private research centers.

L'archive ouverte pluridisciplinaire **HAL**, est destinée au dépôt et à la diffusion de documents scientifiques de niveau recherche, publiés ou non, émanant des établissements d'enseignement et de recherche français ou étrangers, des laboratoires publics ou privés.

HAL Authorization

# High-conducting $Bi_4V_{1.8}Cu_{0.2-x}Sb_xO_{10.7+3x/2}$ ceramics: Structural, microstructural, electrical and optical properties

W. Mhaira [a], A. Agnaou [a], R. Essalim [a], F. Mauvy [b,*], M. Zamama [a], M. Alga [a], A. Ammar [a]

[a] *Laboratory of Materials Science and Process Optimization (SCIMATOP), Cadi Ayyad University, Faculty of Science-Semlalia, Av. My Abdellah, B.P. 2390, Marrakech, Morocco*

[b] *CNRS, Université de Bordeaux, (ICMCB), UMR 5026, 87, Av. Dr A. Schweitzer, 33608, Pessac, France*

*Keywords:*
BiCuSbVOx
XRD
FT-IR
Optical properties
And ionic conductivity

A B S T R A C T

The partial substitution of copper by antimony in $Bi_4V_{1.8}Cu_{0.2}O_{10.7}$ compounds leds to the solid solution $Bi_4V_{1.8}Cu_{0.2-x}Sb_xO_{10.7+3x/2}$ ($0.00 \leq x \leq 0.20$). X-ray diffraction and thermal analysis showed that for all compositions, the obtained phases are isotype to the tetragonal γ or γ′ form of $Bi_4V_2O_{11}$. The effect of $Sb^{5+}$ doping on electrical conductivity was studied using electrochemical impedance spectroscopy in the temperature range 200–700 °C. The changes in slope observed in the Arrhenius plots correspond to the structural transitions that occur within the material. The band gap was determined by DRS spectra, BiCuSbVOx materials have a very low gap band (1.77–1.80 eV) compared to parent phase $Bi_4V_2O_{11}$ and the most of BIMEVOX semiconductor materials. The band located around 860 $cm^{-1}$ in Raman spectroscopy is attributed to V–O bond and more especially to $V–O_2$ bond.

## 1. Introduction

The bismuth vanadate $Bi_4V_2O_{11}$ is a member of the Aurivillius homologous series $(Bi_2O_2)(A_{n-1}B_nO_{3n+1})$ with n = 1. $Bi_4V_2O_{11}$ has been highlighted since the last 1980s because of their interesting electrical properties, in particular the conduction by oxygen ions $O^{2-}$ [1].

The crystal structure of de $Bi_4V_2O_{11}$ is constituted by an interlayer growth $(Bi_2O_2)^{2+}$ and pérovskite type layers $(VO_{3.5})^{2-}$. $Bi_4V_2O_{11}$ present three thermodynamically stable crystallographic polymorphs α, β et γ. When heating the phase α- $Bi_4V_2O_{11}$ stable at room temperature, turns into β and then into γ - $Bi_4V_2O_{11}$. This last form is characterized by a disorder of oxygen vacancies in the layers $(VO_{3.5})^{2-}$ [2,3]. This disorder is responsible for the high conductivity observed in this polymorph (0.2 S. $cm^{-1}$ à 600 °C) [1]. Thus, for this reason, many studies have been carried out in recent years to stabilize the most conductive γ - $Bi_4V_2O_{11}$ phase at room temperature, which led to the preparation of a new family of compounds known by the acronym BiMeVOx with the de formula $Bi_4V_{2-x}M_xO_{11-\delta}$, obtained from the partial substitution of vanadium with cations in the parent phase $Bi_4V_2O_{11}$. These materials have several interesting applications, such as their use in electrochemical oxygen pumps, oxygen sensors, catalytic membranes or in fuel cells [4–6]. In 1990, Abraham et al. succeeded in stabilizing the γ-polymorph by doping $Bi_4V_2O_{11}$ with copper, resulting in a new solid solution BiCuVOx. In this system, the compound with a $V^{5+}$ degree of substitution of 10% has the best electrical conductivity [7]. Some works concern the double substitution of $V^{5+}$ ions by iso/aliovalent cations, the solid solutions are formulated by $Bi_4V_{1.8}M_{0.2-x}M'_xO_{11}$ [8–12]. However, the mono- and bi-substituted phases can occur, at low temperatures, in the form of a pseudomorph of the γ-form, denoted γ'. Such phases can be obtained by the partial ordering of the anionic vacancies. The γ′ form has a lower conductivity and higher activation energy than those of the γ. On the other hand, the use of substituted BIMEVOX semiconductor materials is a method for improving the structural, microstructural, electrical, optical, and photocatalytic properties, which means their applicability to various fields. Due to its relatively narrow band gap (2.4–2.9 eV), bismuth and vanadium oxide ($Bi_4V_2O_{11}$) is a semiconductor that reacts with visible light and can absorb sunlight. Therefore, we can solve a very interesting environmental problem by the photocatalytic degradation of industrial pollutants from various factories (pharmaceutical, chemical, petrochemical …) The substitution by transition metals or rare earths in the mother phase $Bi_4V_2O_{11}$ improves their optical absorption, reduces the band gap and makes them useable for photocatalytic applications.

In the present work, the study of copper substitution in $Bi_4V_{1.8-}Cu_{0.2}O_{10.7}$ by $Sb^{5+}$ cations is undertaken. Indeed, the monosubstituted

* Corresponding author.
*E-mail address:* fabrice.mauvy@icmcb.cnrs.fr (F. Mauvy).

phases by copper and by antimony present high values of ionic conductivity σ ($Bi_4V_{1.8}Cu_{0.2}O_{10.7}$) = 4.16 × $10^{-2}$ S $cm^{-1}$ à 600 °C [6] and σ ($Bi_4V_{1.7}Sb_{0.3}O_{11}$) = $10^{-2}$ S $cm^{-1}$ à 317 °C [13].

## 2. Experimental

During the synthesis process, the reagents $Sb_2O_5$ (Merck, 99.99%), $Bi_2O_3$ (Merck, 99.5%), $V_2O_5$ (Merck, 99%) and CuO (Merck, 98%) are first dried, then weighed in stoichiometric proportions. The reaction mixture is then intimately ground in an agate mortar. The powder obtained is placed in a platinum crucible and heated for 24 h at 800 °C. The rate of temperature increase is about 5 °C/min. In order to obtain phases in a state of equilibrium at room temperature, a slow cooling to room temperature is carried out with a rate of 2 °C/min. Three heat treatments interspersed with grinding were sufficient to obtain pure phases.

The powdered samples were characterized by X-ray diffraction using a Rigaku diffractometer, Smart Lab, using a copper anticathode ($\lambda K_\alpha$ = 1.5418 Å). Diffractograms were recorded for 2θ angles between 10 and 70°, using increments of 0.02°. Lattice parameters were calculated using the Fullprof program (Dicvol 6). The γ phase was modeled in space group I4/mmm with approximate mesh parameters a = 3.93 Å and c = 15.54 Å.

Structure refinement of $Bi_4V_{1.8}Cu_{0.15}Sb_{0.05}O_{10.625}$ phase was carried out by Rietveld method using Fullprof-suite software. Data were modeled using a tetragonal mean subcell in space group I4/mmm with a starting model based on the structure of γ-BICOVOX with approximate cell dimensions a≈3.92 Å and c ~ 15.44 Å.

Differential Thermal Analysis (DTA) experiments were conducted on all samples using a LABSYS Evo TGA 1600 analyzer. The temperature range spanned from 25 °C to 750 °C, employing a heating rate of 10 °C/min.

The synthesized powder was dispersed in dried potassium bromide KBr (99% KBr and 1% samples) and the mixture was compressed under vacuum to prepare pellets for infrared spectroscopy analysis. Using a Burker VERTEX 70 FTIR spectrometer in transmission mode, the pellets obtained were analyzed in the frequency range from 400 to 4000 cm-1.

Raman scattering spectra of the pellet samples were captured using the Confotec MR520 spectrometer. An argon ionized laser emitting in the green at wavelength λ = 532 nm was used for these measurements.

The electrical conductivity of the samples was evaluated using the Electrochemical Impedance Spectroscopy (EIS) technique. The measurements were conducted over a frequency range of 0.01–1 MHz using an AUTOLAB PGSTAT 302 instrument. A sinusoidal AC signal with an amplitude of 50 mV was applied to the samples. The experiments were carried out on sintered pellets with a relative density exceeding 90% under steady-state conditions. To prepare the pellets, they were initially heated to 830 °C and held at this temperature for 15 h. Platinum ink electrodes were then deposited on both flat surfaces of the pellets. Impedance measurements were recorded from 120 to 700 °C under dry air conditions, maintaining an isothermal plateau for 60 min. The obtained impedance spectra were subsequently analyzed using electrical equivalent circuits consisting of resistances and Constant Phase Elements (CPE) connected in parallel. The parameters of the circuit elements were determined through non-linear least-square fitting utilizing the Z.View software developed by Scribner Associates.

The UV–visible diffuse reflectance spectra were acquired using a Jasco-770 spectrophotometer equipped with an integrating sphere ILN-925 for diffuse reflectance measurements. The reflectance data obtained were converted to absorbance values. The optical band gap was then determined from the absorbance data using the Tauc plot method, which involves applying Kubelka-Munk's equation.

For the ceramic study, the powder has been ground for 10 min then sieved with a 50 μm sieve and compacted by uniaxial manual pressing (1 ton/$cm^2$) into cylindrical pellets (8 mm diameter and about 2 mm thick). The obtained pellets were sintered at 800 °C for 10 h and cooled slowly to room temperature.

In order to observe the microstructure using scanning electron microscopy (SEM), the faces of the sintered pellets were carefully polished using SiC paper with grit sizes ranging from 1500 to 5000. The polished samples were then analyzed using a scanning electron microscope, specifically the VEGA3 LMU model. To highlight the grain boundaries, thermal etching was employed by subjecting the samples to a temperature of 750 °C around 20–30 min.

## 3. Results and discussion

### 3.1. X rays diffraction characterizations

The X-rays patents recorded at room temperature related to the selected compounds de $Bi_4V_{1.8}Cu_{0.2-x}Sb_xO_{10.7+3x/2}$ ($0.00 \leq x \leq 0.20$), are reported on Fig. 1. The presence of an indexed singlet peak (110) at $2\theta \approx 32°$, suggests the stabilization of the tetragonal structure of the γ - $Bi_4V_2O_{11}$ polymorph at room temperature. Thus, the substitution of copper in $Bi_4V_{1.8}Cu_{0.2}O_{10.7}$ by $Sb^{5+}$ stabilizes the high-temperature variety for all solid solution compositions $Bi_4V_{1.8}Cu_{0.2-x}Sb_xO_{10.7+3x/2}\square_{1.3-3x/2}$ (□ represents oxygen vacancies). $Bi_4V_2O_{11}$ is a member of the Aurivillius $2(Bi_2O_2)^{2+}(A_{n-1}B_nO_{3n+1})^{2-}$ family compounds, whose structure consists of alternating fluorite-like $(Bi_2O_2)^{2+}$ layers and perovskite-like $(A_{n-1}B_nO_{3n+1})^{2-}$ blocks. In the case of $Bi_4V_2O_{11}$ (n = 1), the perovskite-like layers are reduced to a layer of oxygen-deficient octahedra $(VO_{3.5}\square_{0.5})^{2-}$, i.e. $2(Bi_2O_2)^{2+}(VO_{3.5}\square_{0.5})^{2-}$ ($Bi_4V_2O_{11}\square_1$). In the case of substitution of $V^{5+}$ by ions with lower valence, the chemical formula for BiMeVOx is therefore as follows $Bi_4Me_xV_{2-x}O_{11-\delta}\square_{1+\delta}$. The quantities of oxygen vacancies in solid solutions have been calculated according to electrical charge neutrality, using the chemical formula $Bi_4Cu_xV_{2-x}O_{11-3x/2}\square_{1+3x/2}$ (in the present case, x = 0.2, i.e. $Bi_4Cu_{0.2}V_{1.8}O_{10.7}\square_{1.3}$) and $Bi_4V_{1.8}Cu_{0.2-x}Sb_xO_{10.7+3x/2}\square_{1.3-3x/2}$ (in this family of compounds, $0.0 < x \leq 0.2$).

The variations of the crystal lattice parameters as a function of the antimony content are reported in Fig. 2. The evolution of a and c parameters is dependent on two factors involved during the substitution: the decrease of the ionic radius of the dopant ($Sb^{5+}$ (r = 0.60 Å), $Cu^{2+}$ (r = 0.74 Å) [14] and decrease of the level of anionic vacancies. It can be mentioned that at low dopant concentration (x = 0.1), a slight decrease in the volume of the lattice due to a significant contraction of the a-parameter compared to x = 0.0. Then, for increasing x, an increase of the a parameter up to the composition x = 0.15 was observed and can be explained by level of anionic vacancies which are located generally in equatorial positions in BiMeVOx. In the case of x = 0.20 the decrease of the a-parameter may be assigned to the effect of the dopant size which becomes predominant. The same behavior was observed in the case of

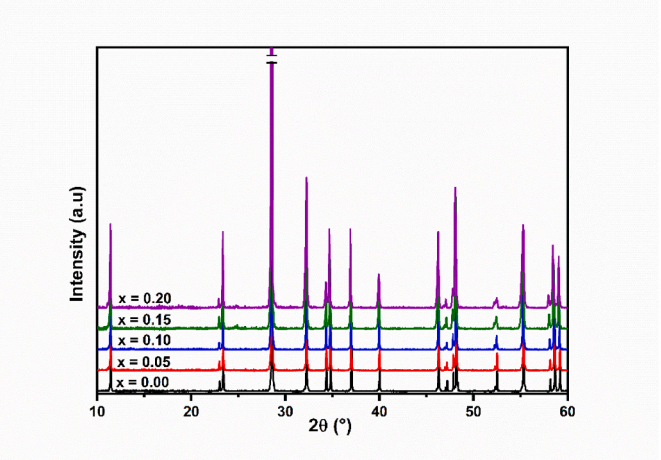


**Fig. 1.** X rays diffraction patents of $Bi_4V_{1.8}Cu_{0.2-x}Sb_xO_{10.7+3x/2}$ phases ($0.00 \leq x \leq 0.20$).

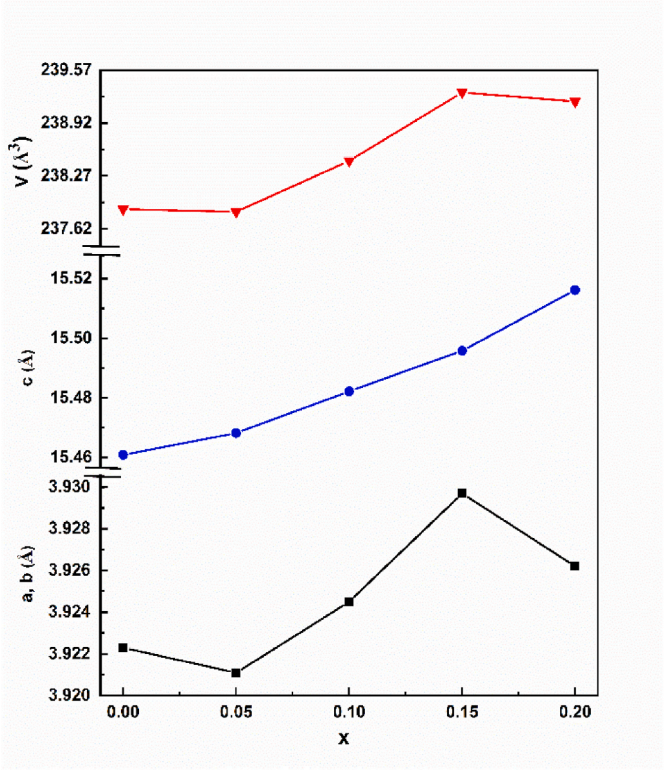


**Fig. 2.** Evolution of the cell parameters and the lattice volume versus the x substitution ratio x in the solid solution solid $Bi_4V_{1.8}Cu_{0.2-x}Sb_xO_{10.7+3x/2}$.

substitution of $Cu^{2+}$ ions by $Al^{3+}$ ions in $Bi_4V_{1.8}Cu_{0.2}O_{10.7}$ where the variation of the parameter a was explained by the competition of the effects of dopant size and level of vacancies in the lattice [11]. The c parameter increases with the degree of substitution over the entire solid solution domain. This unexpected behavior cannot be explained on the basis of the effective ionic radii ($r(Sb^{5+}) < r(Cu^{2+})$), so since the c-axis reflects the distance between the vanadate and bismuthate layers, such a trend seems to indicate the decrease of the interaction between these layers. The same behavior was observed for the $Bi_4V_{2-x}Ge_xO_{11-y}$ solid solution where the size of $Ge^{4+}$ ion is smaller than that of the $V^{5+}$ ion [15].

Fitted XRD profile for $Bi_4V_{1.8}Cu_{0.15}Sb_{0.05}O_{10.625}$ composition with a γ - phase structure, at ambient temperature is shown in Fig. 3. The refined unit cell parameters and the refined atomic parameters are given in Table 1. The Bi–O and V/M − O contact distances are shown in

**Table 1**
Parameters and R-factors for $Bi_4V_{1.8}Cu_{0.15}Sb_{0.05}O_{10.625}$ from the Rietveld refinement.

| Atom | Valence | Site | x | y | z |
|---|---|---|---|---|---|
| Bi1 | 3 | 4e | 0.0000 | 0.0000 | 0.1687 |
| V1 | 5 | 2a | 0.0000 | 0.0000 | 0.5000 |
| Cu1 | 2 | 2a | 0.0000 | 0.0000 | 0.5000 |
| O1 | −2 | 4d | 0.0000 | 0.5000 | 0.2500 |
| O2 | −2 | 16n | 0.0000 | 0.1967 | 0.4041 |
| O3 | −2 | 16n | 0.0000 | 0.4007 | 0.0222 |
| Sb1 | 5 | 2a | 0.0000 | 0.0000 | 0.5000 |

a = 3.919(1) Å c = 15.463(5) Å
Z = 1.
Number of Space group: 139.
Space group: I4/*mmm*.
Volume = 237.510(0) Å$^3$.
The density of the compound: 7.947.
R factors Rp = 10.6% Rwp = 8.9% Rexp = 7.93%.
χ2 = 0.988.

**Table 2**
The M − O bond distances found by the Rietveld refinement (M:Cu/Sb).

| bond length | Distance (Å) |
|---|---|
| (V/M)-($O_2$) | 1.671(1) |
| (V/M)-($O_3$) | 2.027(1) |
| (Bi)-($O_1$) | 2.328(9) |
| (Bi)-($O_2$) | 2.552(9) |
| (Bi)-($O_3$) | 2.577(3) |

Table 2. The crystal structure obtained by the vesta software is given in Fig. 4. The structure is formed by intergrowth of a fluorite-like $Bi_2O_2$ layer and a perovskite-like layer. In the crystallographic model adopted in this study, Bi shows three types of bond to O: the shortest one Bi–O1 in bismuthate layer (2.328 Å), and two longer bonds to oxygen atoms in the vanadate layer Bi–O2 (2.552 Å) and Bi–O3 (2.577 Å). M (V, Cu or Sb) shows two types of contact to O: M-O2 (1.671 Å) and M-O3 (2.027 Å). This result agrees with that of the Raman study, which shows only two bands corresponding to the vibration modes of M − O bonds. The distance M-O2 is consistent with $V^{5+}$ in a tetrahedral coordination ($r_i(V^{5+}) + r_i(O^{2-}) \approx 1.70$ Å [14]) and the distance M-O3 is consistent with $Cu^{2+}$ in octahedral coordination ($r_i(Cu^{2+}) + r_i(O^{2-}) \approx 2.08$ Å [14]).

### 3.2. *Differential Thermal Analysis*

The DTA analysis was performed for the parent compounds $Bi_4V_2O_{11}$ and the $Bi_4V_{1.8}Cu_{0.2-x}Sb_xO_{10.7+3x/2}$ samples with compositions x = 0.05,

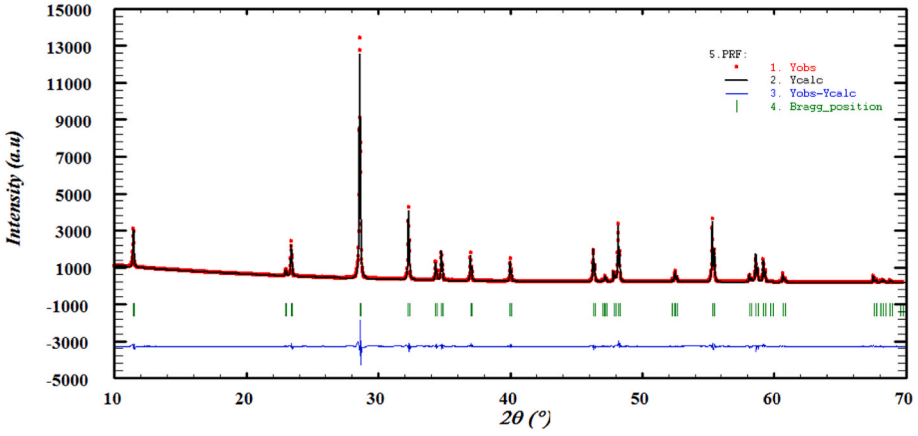


**Fig. 3.** Rietveld refined X-ray pattern of $Bi_4V_{1.8}Cu_{0.15}Sb_{0.05}O_{10.625}$.

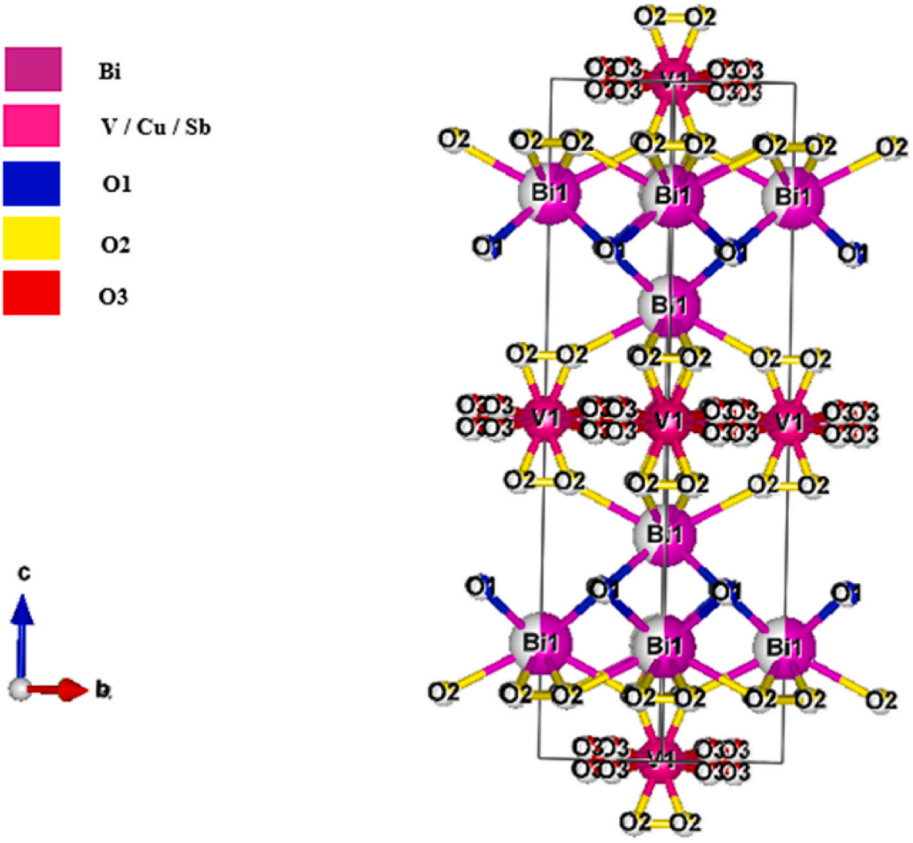


**Fig. 4.** Crystal structure of $Bi_4V_{1.8}Cu_{0.15}Sb_{0.05}O_{10.625}$.

0.10, 0.15 and 0.20. The results of the measurements are shown in Fig. 5. The existence of two endothermic peaks at 447 °C and 531 °C in the DTA curves can be observed for $Bi_4V_2O_{11}$ are attributed to the α→β and β→γ transitions A single endothermic peak, with low intensity, was observed in the temperature around T = 458 °C for the material with x = 0.05. This phenomenon can be attributed to the γ' → γ transition, while no thermal effects have been observed for the compounds with x = 0.10, 0.15, and 0.20 (Fig. 5). The absence of any peak in the plot shows that these phases contain a low level of the γ′ pseudomorph. These results, which are in significant accord with the XRD results, indicate to the double substitution's ability to stabilize the tetragonal form at room temperature.

### 3.3. *Infra-red spectroscopy measurements*

The FT-IR spectra recorded in the frequency range 1200–400 $cm^{-1}$ for different compositions 0.00 ≤ x ≤ 0.20 and for the compound $Bi_4V_2O_{11}$ are shown in Fig. 6.

The characteristic bands of BiMeVOx are found in all spectra. The bands at 440 $cm^{-1}$ and 520 $cm^{-1}$ correspond to the $\nu$ (Bi–O) bond stretching vibrational mode of the bismuth layers in $BiO_6$ octahedral units and the $\nu$ (Bi–O) stretching vibrational mode in distorted $BiO_6$ octahedral units, respectively, which is superimposed on the longitudinal stretching mode of V-$O_A$ ($O_A$: represents the oxygen in apical position in $VO_{3.5}\square_{0.5}$ layers. The bands around 735 $cm^{-1}$ and 817 $cm^{-1}$ have

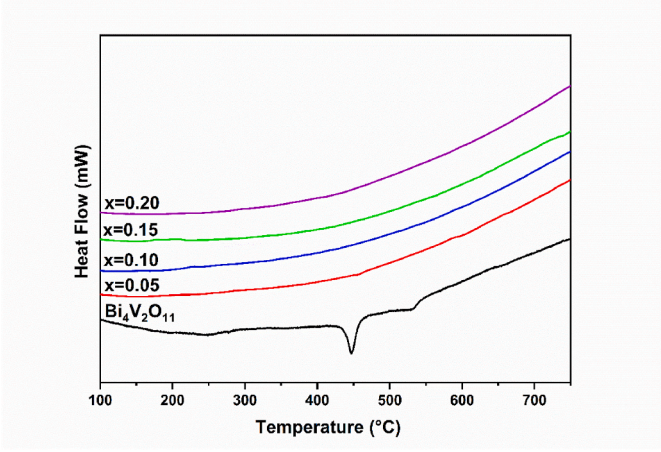


**Fig. 5.** DTA curves of $Bi_4V_2O_{11}$ and selected compounds x = 0.05, 0.10, 0.15, 0.20 in the solid solution $Bi_4V_{1.8}Cu_{0.2-x}Sb_xO_{10.7+3x/2}$.

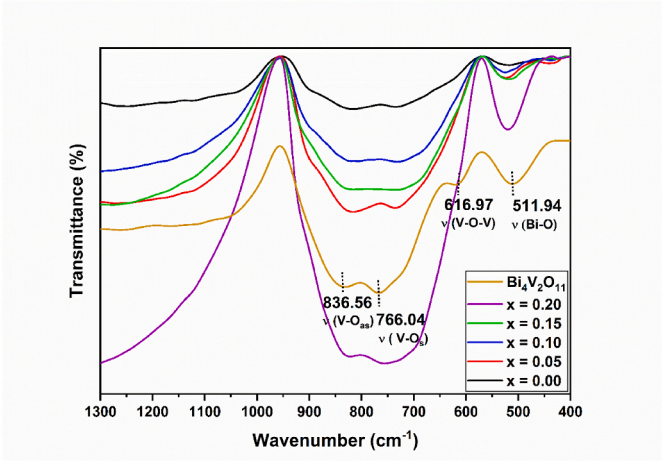


**Fig. 6.** FT-IR spectra of the compounds $Bi_4V_{1.8}Cu_{0.2-x}Sb_xO_{10.7+3x/2}$ (0.00 ≤ x ≤ 0.20).

been assigned to the symmetrical stretching vibration $v_s$(V–O) and to the asymmetrical stretching $v_{as}$(V–O) respectively [13]. These latter bands are wider than those observed for the parent compound $Bi_4V_2O_{11}$. This indicates crystallographic disorder in the BiCuSbVOx system that evolves with the doping level. Examination of the FT-IR spectra show that some bands shift to low or high frequencies, while others disappear completely from the spectrum depending on the composition as shown in Table 3. These observations confirm the substitution of copper by antimony. Thus the absence of the $v_{as}$(V–O) band for some compositions (Table .3), suggests a high degree of crystallographic disorder as previously observed in the case of the compounds BiTiNbVOx [15,16].

The $v_s$(V–O) and $v_{as}$(V–O) bands are clearly defined for the compound $Bi_4V_2O_{11}$, indicating an ordered crystal structure. However, for the BiCuSbVOx system, the broadening of the $v_s$ (V–O) band indicates a disorder in the network confirmed by the near disappearance of the $v_{as}$ (V–O) band in the spectrum for some compositions (x = 0.00 and x = 0.15).

### 3.4. Raman spectroscopy analysis

The Raman spectra measured at room temperature for the compounds $Bi_4V_{1.8}Cu_{0.2-x}Sb_xO_{10.7+3x/2}$ in the substitution range $0.00 \leq x \leq 0.20$ are reported in Fig. 7. The signals between 300 and 860 $cm^{-1}$ are associated to V–O modes, including bending (360–369 $cm^{-1}$), symmetric stretching (ca. 500 $cm^{-1}$) and asymmetric stretching (600–860 $cm^{-1}$) vibrations.

All spectra show a similarity of some overlapping bands in the spectral range of 600–900 $cm^{-1}$ as dominant characteristic bands. The main Raman bands in this region, have been attributed to symmetric and asymmetric stretching vibrations of the V–O bonds in the $VO_4$ polyhedra. For the compositions x = 0.15 and x = 0.20, the appearance of a band around 922 $cm^{-1}$ which becomes visible for an increasing antimony content can be noticed. This band can be attributed to short V═O terminal bond elongation vibrations [17–19].

Raman spectroscopy measurements was used to estimate the V–O bond length (R (Å)) from Raman spectra in the frequency range 400–1200 $cm^{-1}$. For this purpose, an empirical equation, established by Hardcastle and Wachs [20], was applied.

From a large number of experimental data for compounds containing V–O bonds, Hardcastle and Wachs correlated Raman frequencies with V–O bond lengths in vanadium oxide compounds. The method uses the diatomic approximation, which assumes that each separate metal-oxygen bond vibrates independently of the crystal lattice. The associated relation is as follows:

$$\nu = 21349 \times \exp(-1.9176 \times R) \quad (1)$$

The V–O bond lengths, denoted by the letter R, calculated from Equation (1), are given in Table 4. The dependence of R on composition highlights the local changes affecting the V–O bond environment. For $x \leq 0.15$, it can be noticed that R has the same type of variation as the a and c lattice parameters as a function of composition. The increase of R can be explained by the decrease of the level of anionic vacancies and the increase of the vanadium coordination for increasing x. The value of V–O bond lengths obtained from Raman spectroscopy is the same obtained for the V–O2 distances from the crystallographic study, so we can also conclude from the results of the Rietveld refinement (Table 2) that

**Table 3**
Bi–O and V–O infrared vibrational frequencies.

| Composition | Bi–O ($cm^{-1}$) | Bi–O/V-$O_A$ ($cm^{-1}$) | V–O ($cm^{-1}$) | V–O ($cm^{-1}$) |
|---|---|---|---|---|
| 0.00 | 428.63 | 520.01 | 733.60 | – |
| 0.05 | 439.58 | 523.11 | 735.06 | 815.68 |
| 0.10 | 436.47 | 524.57 | 730.50 | 820.06 |
| 0.15 | 425.53 | 516.91 | 730.50 | – |
| 0.20 | 419.33 | 520.02 | 753.67 | 823.34 |

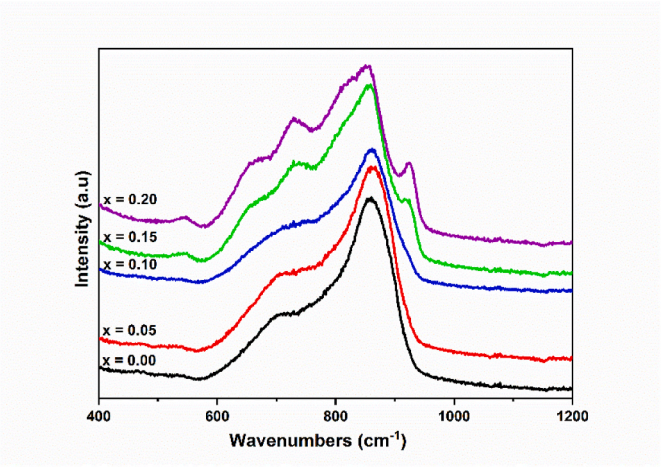


**Fig. 7.** RAMAN spectra of the compounds $Bi_4V_{1.8}Cu_{0.2-x}Sb_xO_{10.7+3x/2}$ ($0.00 \leq x \leq 0.20$).

**Table 4**
The V–O bond distances estimated from Raman bands.

| x | $\nu$ ($cm^{-1}$) | R (Å) |
|---|---|---|
| 0.00 | 859 | 1.6755 |
| 0.05 | 863 | 1.6731 |
| 0.10 | 861 | 1.6743 |
| 0.15 | 858 | 1.6761 |
| 0.20 | 854 | 1.6785 |

the band located around 860 $cm^{-1}$ can be attributed to the vibration of the V–O2 bond in $VO_4$ polyhedron in the crystallographic model adopted.

### 3.5. Microstructure characterization by SEM images

The SEM micrographs of the compounds $Bi_4V_{1.8}Cu_{0.2-x}Sb_xO_{10.7+3x/2}$ with $0.00 \leq x \leq 0.20$ are reported on Fig. 8. The morphology of the ceramics differs according to their composition. The SEM micrographs show well defined grains and well visible grain boundaries for all the ceramics studied. A relatively uniform grain size distribution is observed. The increase of the antimony degree of substitution is accompanied by a decrease of the grain size and an increase of the porosity which is located along the grain boundaries. Indeed, the substitution of $Cu^{2+}$ by $Sb^{5+}$ is associated to a decrease in the level of anionic vacancies which leads to a decrease in the diffusion of ions. The substitution ratio x = 0.05 seems to be the optimal composition which allows both grain growth and better densification.

### 3.6. Ionic conductivity measurements

The Electrochemical Impedance Spectroscopy (EIS) analysis were carried out on pellets sintered at 800 °C for 10 h in air. The studied samples have a relative density of about 89%. Fig. 9 shows typical impedance diagrams for the $Bi_4V_{1.8}Cu_{0.2-x}Sb_xO_{10.7+3x/2}$ solid solution. The impedance diagrams in the Nyquist plane consist of a single depressed semicircle for all compositions studied. Unlike most materials with oxygen ion conductivity that exhibit two semicircular contributions, the EIS diagrams are characterized by a single arc that reflects an overlapping effect of both grain interior and grain boundary contributions. A straight line is observed at low frequencies corresponding to the phenomenon of polarization of the electrode due to ion blocking process at the noble metal surface. This is the reason why an equivalent circuit based on a R//CPE elements associated with a low frequency Warburg-type impedance has been selected for data modelling (see insert Fig. 9).

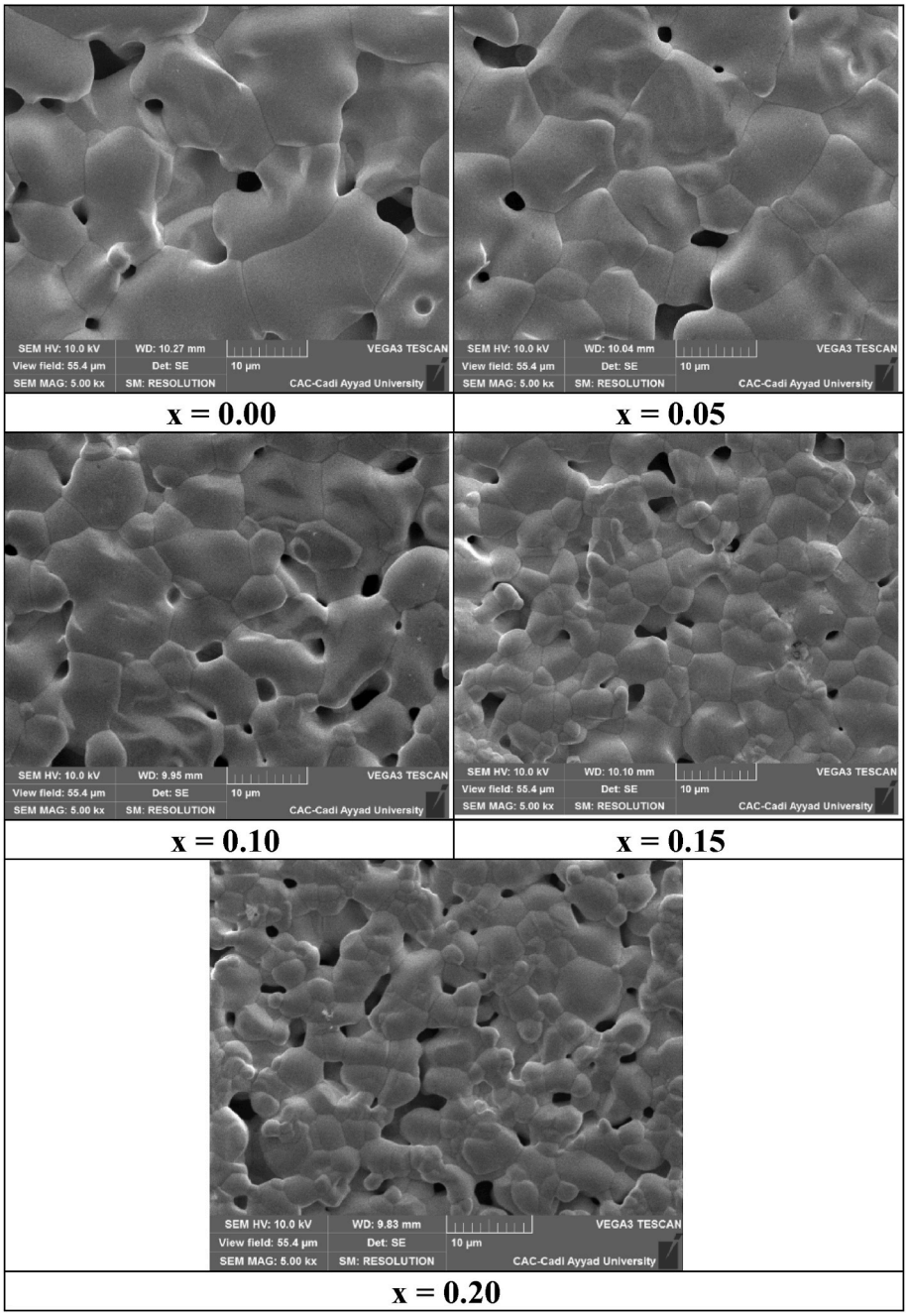


**Fig. 8.** SEM micrographs of selected compounds $Bi_4V_{1.8}Cu_{0.2-x}Sb_xO_{10.7+3x/2}$ with x = 0.00, 0.05, 0.10, 0.15 and 0.20.

It can be observed that the modification of the antimony content leads to a shift in the plots and a change in the diameters of the semicircles.

The logarithm of conductivity versus the reverse of the working temperature log (σ) = f (1000/T) is given in Fig. 10 for different compositions. The samples show straight lines of the Arrhenius type according to a thermally activated process. A change in slope is observed in the temperature range between 495 and 527 °C, which can be related to the γ→γ′ order/disorder transformation [21]. This result is in good agreement with those of XRD and DTA. It is clear that the double substitution of vanadium by copper and antimony increases the stability range of the γ phase to lower temperatures at the expense of the less conductive γ′ phase (Table 5). In the high temperature range, a decrease in conductivity is observed for increasing copper substitution rates (Table 5). This behavior may be related to the decrease in the rate of oxygen vacancies that contribute in $O^{2-}$ ionic transport, therefore $Bi_4V_{1.8}Cu_{0.2}O_{10.7}$ shows the best conductivity at high temperature ($\sigma_{600°C}$ = 2.19 $10^{-2}$ S/cm). In addition, the microstructure of ceramics can also affect the conductivity. Indeed, in polycrystalline compounds, increasing grain size often decreases the contribution of grain boundaries to resistivity and thus favors oxygen vacancy transport [22]. For this purpose, the SEM micrographs (Fig. 8) corresponding to the compositions x = 0.00, x = 0.05 and x = 0.10, presenting less porosity and larger grains, are therefore, more conductive at high temperatures. At low temperature, the conductivity is significantly higher for the doubly substituted phases than for the monosubstituted phases $Bi_4V_{1.8}Cu_{0.2}O_{10.7}$ and $Bi_4V_{1.8}Sb_{0.2}O_{11}$ (Table 5). This result highlights the role of double substitution in creating disorder in the crystal lattice. A comparison of the conductivity of the BiCuSbVOx double-substituted phases with that of the reference electrolyte used so far, the yttria stabilized zirconia YSZ [23] shows that these ceramic compounds perform

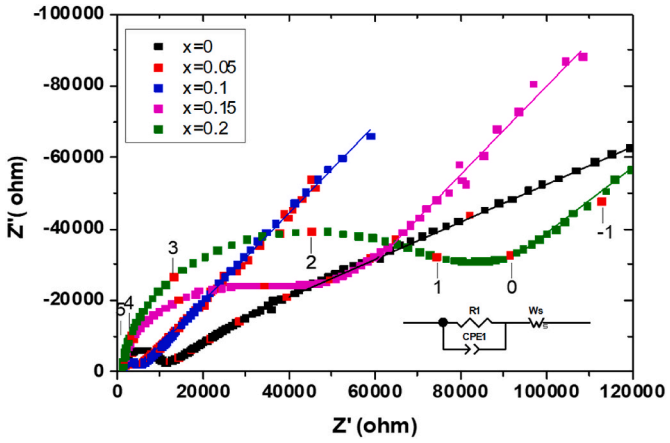


**Fig. 9.** Typical Nyquist diagrams of ceramic compounds $Bi_4V_{1.8}Cu_{0.2-x}Sb_xO_{10.7+3x/2}$ recorded at 300 °C, under air. The numbers inside are the frequencies logarithm. The selected equivalent circuit is also inserted in the figure.

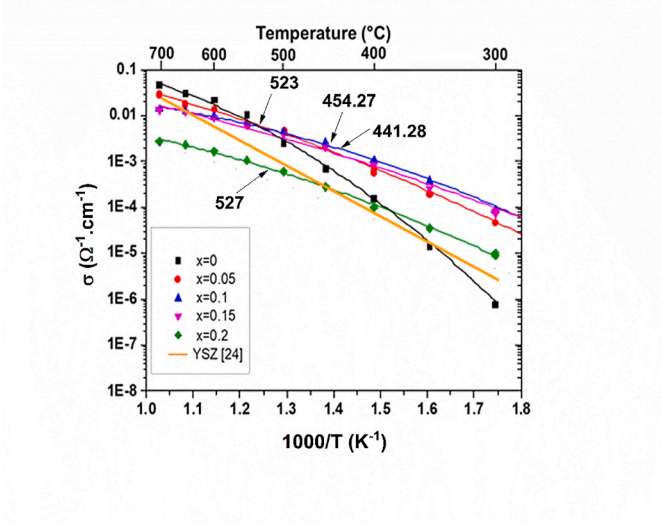


**Fig. 10.** Ionic conductivity Arrhenius plots of $Bi_4V_{1.8}Cu_{0.2-x}Sb_xO_{10.7+3x/2}$ compounds and YSZ (as reference material).

**Table 5**
Ionic conductivity values and activation energy of the $Bi_4V_{1.8}Cu_{0.2-x}Sb_xO_{10.7+3x/2}$ ceramics.

| x | $\sigma_{600°C}$ (S.cm$^{-1}$) | $\sigma_{300°C}$ (S.cm$^{-1}$) | $Ea_{HT}$(eV) T > 600K | $Ea_{IT}$(eV) T < 600K | $T_{\gamma-\gamma'}$ (°C) |
|---|---|---|---|---|---|
| **0.00** | $2.19 \times 10^{-2}$ | $1.13 \times 10^{-6}$ | 0.74 | 1.42 | 523 |
| **0.05** | $1.392 \times 10^{-2}$ | $1 \times 10^{-4}$ | 0.71 | 0.94 | 454.27 |
| **0.10** | $9.53 \times 10^{-3}$ | $1.33 \times 10^{-4}$ | 0.31 | 0.82 | 441.28 |
| **0.15** | $8.9 \times 10^{-3}$ | $1.2 \times 10^{-4}$ | 0.31 | 0.71 | 441.28 |
| **0.20** | $1.64 \times 10^{-3}$ | $1.07 \times 10^{-5}$ | 0.56 | 0.68 | 527 |

better.

Furthermore, the evolution of the half-value width (FWHM) of the band located around 500 cm$^{-1}$ in the FT-IR spectra and that of the activation energy at low temperature are represented in Fig. 11. The FWHM increases with the degree of substitution x which confirms that the oxygen environment is changed upon substitution. Thus, the width at the midpoint of the band informs about the increase in the local disorder of the oxygen atoms of the Bi–O bond. This highlights the effect of substitution in the perovskite layers on the Bi–O bonds and shows that the $BiO_6$ and $VO_6$ units do not vibrate independently of each other. A

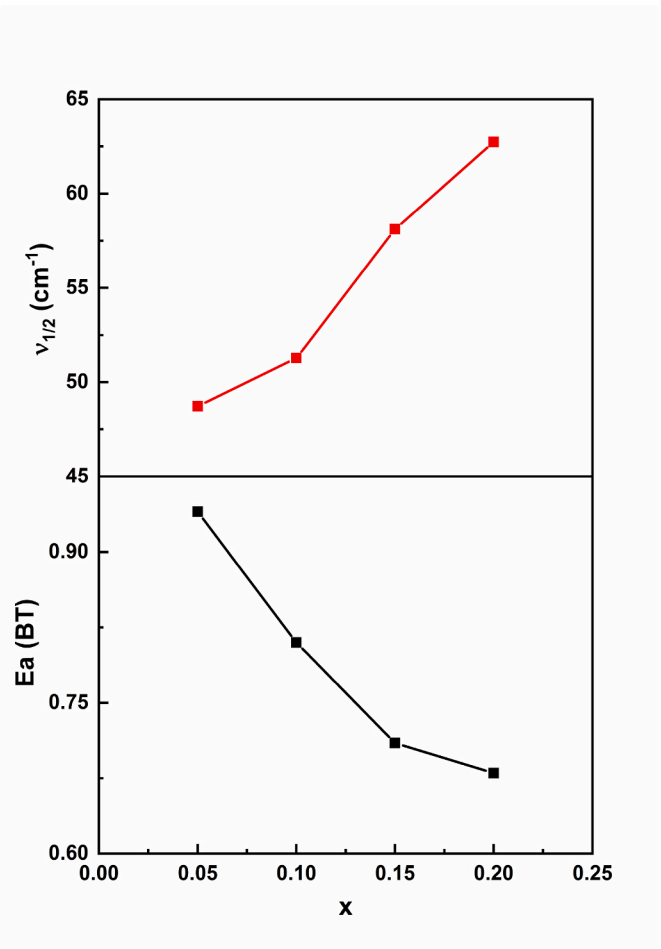


**Fig. 11.** Evolution of the activation energy and of the width at half-height of the IR band located at 500 cm$^{-1}$ as a function of x substitution ratio in the family compounds.

similar behavior in the case of the solid solution BiCuAlVOx have been observed [12]. Furthermore, the half-value width of this band and the activation energy for the doubly substituted BiCuSbVOx phases vary in opposite directions as a function of the antimony content. Assuming that this band can be assigned to the Bi-$O_A$/V-$O_A$ vibrations, the disorder in the position of the apical oxygen $O_A$ (O2 in the crystallographic model) can contribute to the band broadening.

### 3.7. UV–vis diffusion reflectance spectra (DRS)

Fig. 12-a shows the DRS spectra of the synthesized BiCuSbVOx powder samples in the 200–700 nm wavelength range. The results indicated that the BiCuSbVOx samples ($0.00 \leq x \leq 0.15$) show an absorption edge at ≈ 470 nm. Furthermore, the light absorption intensity of the BiCuSbVOx was found to be maximal for the compound with composition $x = 0.10$, indicating significant absorption in the UV–visible light ranges.

The characteristics of the optical inter-band transition and the values of optical band energy gap (Eg) were determined by the Tauc's using Eq. (2) [24].

$$A.h.\nu = A\,(h\nu\text{-}Eg)^{n/2} \quad (2)$$

Where α, υ,h, A, and Eg stand for absorption coefficient, light frequency, Planck constant, absorption constant and bandgap energy, respectively. In this equation, n is governed by the kind of optical transition characteristics of the semiconductor (generally, $n = 1/2$ for a direct transition and $n = 2$ for an indirect transition), $n = 1/2$ for this study.

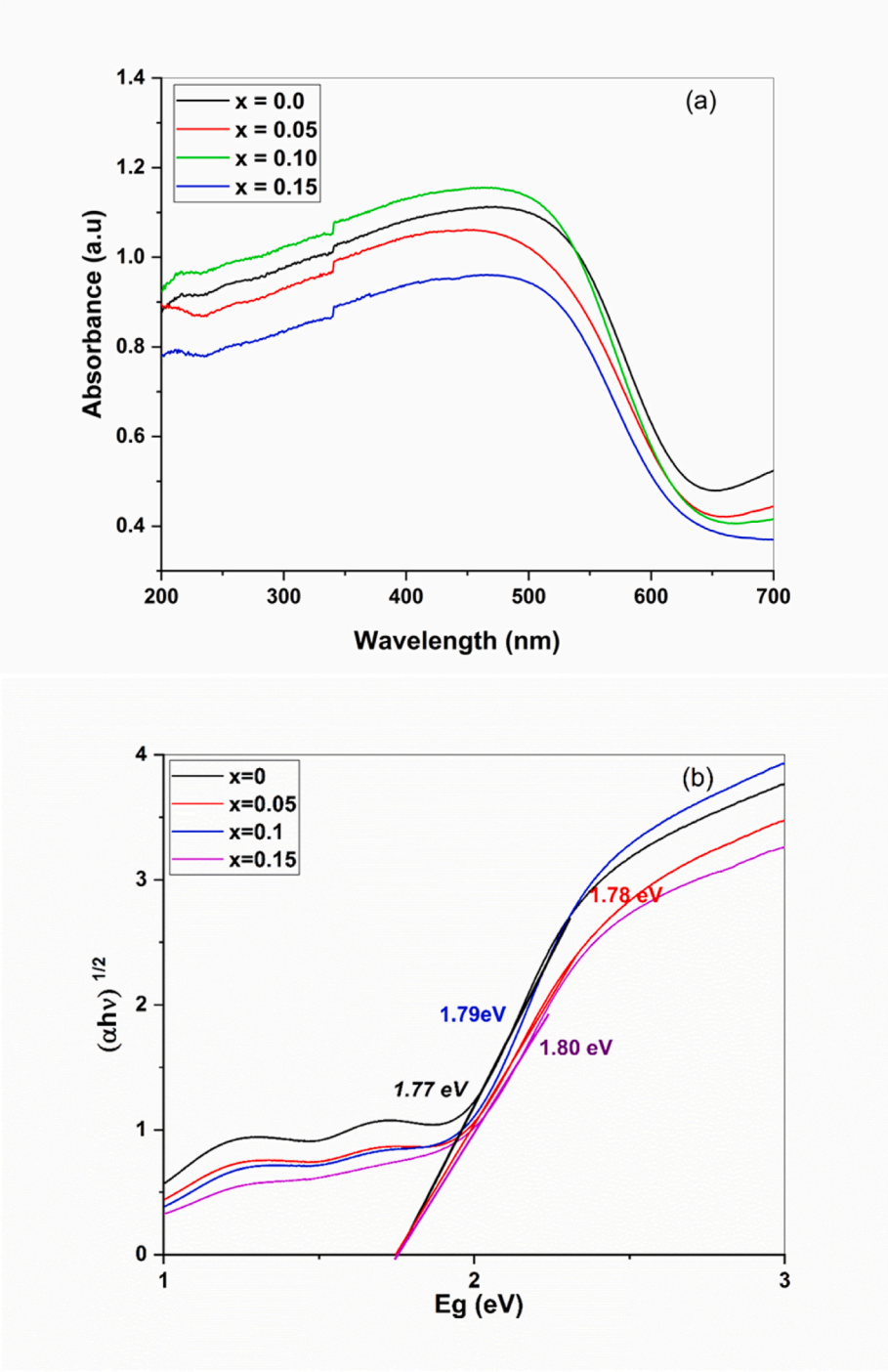


**Fig. 12.** DRS spectra of BiCuSbVOx in the range 200–700 nm and (b) The calculated band gap with the help Tauc plot.

In the plots of $(\alpha h\upsilon)^{1/2}$ vs Eg (Fig. 12-b), the tangents to these curves intercept the X axis at the values of band gap energies between 1.77 and 1.80 eV.

Compared to $Bi_4V_2O_{11}$ (Eg = 2.86 eV) [25], $Bi_4V_{1.8}Cu_{0.2-x}Sb_xO_{10.7+3x/2}$ (x = 0.00) exhibits the highest absorption and lowest Eg value (for $Bi_4V_{1.8}Cu_{0.2}O_{10.7}$(x = 0.00), Eg = 1.77 eV). Which may be due to oxygen vacancies created when $V^{5+}$ ions are replaced by $Cu^{2+}$ ions in the $Bi_4V_2O_{11}$ lattice, which can produce intermediate defect energy levels in the band gap.

For $Bi_4V_{1.8}Cu_{0.2-x}Sb_xO_{10.7+3x/2}$, the values of Eg increase when the concentration of $Sb^{5+}$ doping increases, sample with x = 0.00 has a low Eg, this value may be the reason why this compound has à highest conductivity value compared to other samples. The transition of electrons from the valence band (VB) to the conduction band (CB) was slowed down by the intermediate energy levels, resulting in a narrowing of the band gap. Because of the restricted band gap, BiCuSbVOx may be photoexcited to produce more photoinduced charge transport carriers when exposed to visible light, which can result in enhanced photocatalytic activity. It is clear that photocatalytic degradation performance would be improved by substitution compared to $Bi_4V_2O_{11}$ [26].

## 4. Conclusion

The objective of the present study was the development and

characterization of the series of low dimensional compounds $Bi_4V_{1.8}Cu_{0.2-x}Sb_xO_{10.7+3x/2}$ by substitution of copper (II) with antimony (V) in the compound $Bi_4V_{1.8}Cu_{0.2}O_{10.7}$. The stabilization at room temperature, of the tetragonal variety has been demonstrated throughout the compositional range $0.00 \leq x \leq 0.20$. The change in conductivity values as a function of composition, is in good agreement with the level of anionic vacancies and the microstructure of the ceramics studied. The compositions $x = 0.00$, $x = 0.05$ and $x = 0.10$ show the best microstructural and electrical properties. Moreover, in the whole range of studied temperature, the double substitution of vanadium by copper and antimony leads to a significant improvement of the conductivity compared to the two compounds mono-substituted with copper ($x = 0.00$) and antimony ($x = 0.20$). The DRS spectra show that the BiCuSbVOx solid solution as a function of x has a weak band gap in the range of $1.77\ eV \leq Eg \leq 1.80\ eV$. Overall, it can be concluded that the microstructural, optical and electrical properties of $Bi_4V_{1.8}Cu_{0.2}O_{10.7}$ are improved by the partial substitution of $Cu^{2+}$ by $Sb^{5+}$.

## Declaration of competing interest

The authors declare that they have no known competing financial interests or personal relationships that could have appeared to influence the work reported in this paper.

## Acknowledgments

The authors are grateful to the Cadi Ayyad University Analysis and Characterization Center (CAC) for providing them with materials characterization techniques. They thank also ICMCB Bordeaux for EIS measurements.

## References

[1] F. Abraham, M.F. Debreuille-Gresse, G. Mairesse, G. Nowogrocki, Phase transitions and ionic conductivity in $Bi_4V_2O_{11}$ an oxide with a layered structure, Solid State Ionics 28–30 (1988) 529–532, https://doi.org/10.1016/S0167-2738(88)80096-1.

[2] G. Mairesse, P. Roussel, R.N. Vannier, M. Anne, C. Pirovano, G. Nowogrocki, Crystal structure determination of α, β and γ- $Bi_4V_2O_{11}$ polymorphs. Part I: γ and β-$Bi_4V_2O_{11}$, Solid State Sci. 5 (2003) 851–859, https://doi.org/10.1016/S1293-2558(03)00015-3.

[3] G. Mairesse, P. Roussel, R.N. Vannier, M. Anne, G. Nowogrocki, Crystal structure determination of α-, β- and γ-$Bi_4V_2O_{11}$ polymorphs. Part II: crystal structure of α-$Bi_4V_2O_{11}$, Solid State Sci. 5 (2003) 861–869, https://doi.org/10.1016/S1293-2558(03)00016-5.

[4] J.C. Boivin, C. Pirovano, G. Nowogrocki, G. Mairesse, P. Labrune, G. Lagrange, Electrode-electrolyte BIMEVOX system for moderate temperature oxygen separation, Solid State Ionics 113–115 (1998) 639–651, https://doi.org/10.1016/s0167-2738(98)00330-0.

[5] G. Mairesse, Advances in oxygen pumping concept with BIMEVOX, Comptes Rendus l'Académie Des Sci. - Ser. IIC - Chem. 2 (1999) 651–660, https://doi.org/10.1016/s1387-1609(00)88579-5.

[6] E.S. Buyanova, Z.A. Michaylovkaya, M.V. Yurchenko, O.A. Lipina, Photocatalytic characteristics of complex oxides $Bi_4V_{1.8}Me_{0.2}O_{11-d}$ (me = Co, Cu, Fe, Mn, Nb), Russ. J. Phys. Chem. A 94 (2020) 2527–2533, https://doi.org/10.1134/S0036024420120067.

[7] F. Abraham, J.C. Boivin, G. Mairesse, G. Nowogrocki, The bimevox series: a new family of high performances oxide ion conductors, Solid State Ionics 40–41 (1990) 934–937, https://doi.org/10.1016/0167-2738(90)90157-M.

[8] M.H. Paydar, A.M. Hadian, G. Fafilek, Studies on preparation, characterisation and ion conductivity of Ti-Cu double substituted $Bi_4V_2O_{11}$, J. Eur. Ceram. Soc. 21 (2001) 1821–1824, https://doi.org/10.1016/S0955-2219(01)00123-6.

[9] M. Alga, A. Ammar, R. Essalim, B. Tanouti, A. Outzourhit, F. Mauvy, R. Decourt, Study on structural, thermal, sintering and conductivity of Cu-Co doubly substituted $Bi_4V_2O_{11}$, Ionics 11 (2005) 81–86, https://doi.org/10.1007/BF02430405.

[10] D. Tripathy, J. Saikia, A. Saikia, A. Pandey, On the structure and ionic conductivity of $Bi_2V_{1-x}Ti_{x/2}Gd_{x/2}O_{5.5-\delta}$ system, Phys. B Condens. Matter 627 (2022), 413596, https://doi.org/10.1016/j.physb.2021.413596.

[11] R. Essalim, A. Ammar, B. Tanouti, F. Mauvy, Synthesis, thermal and electrical properties of Al-doped $Bi_4V_{1.8}Cu_{0.2}O_{10.7}$, J. Solid State Chem. 240 (2016) 122–125, https://doi.org/10.1016/j.jssc.2016.05.026.

[12] R. Essalim, A. Ammar, M. Zamama, F. Mauvy, A study on structural properties, conductivity and FT-IR spectroscopy of Cu–Al doubly substituted $Bi_4V_2O_{11}$, J. Solid State Chem. 288 (2020), 121405, https://doi.org/10.1016/j.jssc.2020.121405.

[13] O. Joubert, A. Jouanneaux, M. Ganne, R. Vannier, G. Mairesse, Solid phase synthesis and characterization of new BIMEVOX series: $Bi_4V_{2-x}M_xO_{11}$ (M=Sbv, Nbv), Solid State Ionics 73 (1994) 309–318, https://doi.org/10.1016/0167-2738(94)90049-3.

[14] R.D. Shannon, Revised effective ionic radii and systematic studies of interatomic distances in halides and chalcogenides, Acta Crystallogr., Sect. A 32 (1976) 751–767, https://doi.org/10.1107/S0567739476001551.

[15] Y. Yue, A. Dzięgielewska, S. Hull, F. Krok, R.M. Whiteley, H. Toms, M. Malys, M. Zhang, H. Yan, I. Abrahams, Local structure in a tetravalent-substituent BIMEVOX system: BIGEVOX, J. Mater. Chem. A 10 (2022) 3793–3807, https://doi.org/10.1039/D1TA07547K.

[16] D. Tripathy, A. Saikia, A. Pandey, Effect of simultaneous Ti and Nb doping on structure and ionic conductivity of $Bi_2V_{1-x}Ti_{x/2}Nb_{x/2}O_{5.5-\delta}$ ($0.1 \leq x \leq 0.25$) ceramics, Ionics 25 (2019) 2221–2230, https://doi.org/10.1007/s11581-018-2622-3.

[17] G. Busca, G. Ricchiardi, D.S.H. Sam, J.C. Volta, Spectroscopic characterization of magnesium vanadate catalysts. Part 1. - vibrational characterization of $Mg_3(VO_4)_2$, $Mg_2V_2O_7$ and $MgV_2O_6$ powders, J. Chem. Soc., Faraday Trans. 90 (1994) 1161–1170, https://doi.org/10.1039/FT9949001161.

[18] C. Julien, G.A. Nazri, O. Bergström, Raman scattering studies of microcrystalline $V_6O_{13}$, Phys. Status Solidi 201 (1997) 319, https://doi.org/10.1002/1521-3951(199705)201:1<319::AID-PSSB319>3.0.CO;2-T.

[19] R. Tang, Y. Li, S. Xie, N. Li, J. Chen, C. Gao, P. Zhu, X. Wang, Exploring the coordination change of vanadium and structure transformation of metavanadate $MgV_2O_6$ under high pressure, Sci. Rep. 6 (2016) 1–9, https://doi.org/10.1038/srep38566.

[20] F.D. Hardcastle, I.E. Wachs, Determination of vanadium-oxygen bond distances and bond orders by Raman spectroscopy, J. Phys. Chem. 95 (1991) 5031–5041, https://doi.org/10.1021/j100166a025.

[21] W. Mhaira, A. Agnaou, R. Essalim, A. Turino, F. Mauvy, M. Alga, M. Zamama, A. Ammar, Effect of simultaneous Cu and Nb doping $Bi_4V_2O_{11}$ on structural and electrical properties of $Bi_4V_{2-x}Cu_{x/2}Nb_{x/2}O_{11-3x/4}$, J. Solid State Chem. 320 (2023), 123878, https://doi.org/10.1016/j.jssc.2023.123878.

[22] D. Tripathy, A. Saikia, G.T. Tado, A. Pandey, Role of Al and Ti doping in modulating electrical properties of BIVOX system, J. Adv. Ceram. 8 (2019) 489–499, https://doi.org/10.1007/s40145-019-0329-1.

[23] A. Löfberg, H. Bodet, C. Pirovano, M.C. Steil, R.N. Vannier, E. Bordes-Richard, Catalytic dense membranes of doped $Bi_4V_2O_{11}$ (BIMEVOX) for selective partial oxidation: chemistry of defects versus catalysis, Top. Catal. 38 (2006) 169–179, https://doi.org/10.1007/s11244-006-0082-x.

[24] K. Anwar, F.K. Naqvi, S. Beg, Facile hydrothermal synthesis of Yb doped $Bi_4V_2O_{11}$ nanoparticles for the improvement of photocatalytic and AC impedance performance: investigation of polymorphism, adsorption isotherm, optical properties and possible mechanism with the help of GCMS, J. Alloys Compd. 938 (2023), 168483, https://doi.org/10.1016/j.jallcom.2022.168483.

[25] K. Anwar, F.K. Naqvi, S. Beg, S. Haneef, Photocatalytic degradation of MB dye and paracetamol drug, via hydrothermally synthesised praseodymium doped $Bi_4V_2O_{11}$ nanoparticles, J. Mol. Struct. 1272 (2023), 134183, https://doi.org/10.1016/j.molstruc.2022.134183.

[26] K. Anwar, F.K. Naqvi, S. Beg, Synthesis of tetragonally stabilized lanthanum doped bismuth vanadium oxide nanoparticles and its enhanced visible light induced photocatalytic performance, Phase Transitions 95 (2022) 64–79, https://doi.org/10.1080/01411594.2021.2012175.